The International Journal of Advanced Manufacturing Technology (2019) 100:1043–1054
https://doi.org/10.1007/s00170-018-2330-1

ORIGINAL ARTICLE

Parametric study on influence function in magnetorheological finishing of single crystal silicon

Gourhari Ghosh[1] · Raj K. Dalabehera[1] · Ajay Sidpara[1]

Received: 4 April 2017 / Accepted: 5 June 2018 / Published online: 18 June 2018

Abstract
Magnetorheological finishing (MRF), a precision polishing process, becomes an integral part of optics manufacturing industries for its ability to improve figure and surface finish of complex shape optics without introducing surface damage. It employs magnetically stiffened magnetorheological fluid (MR) ribbon as a flexible polishing tool which moves through the converging gap against workpiece. Material removal characteristic of a polishing tool is described as influence function. Influence function is a parameter to evaluate the efficiency or effectiveness of the polishing process. It provides some useful information for setting up appropriate process parameters to finish different surfaces. Rotational speed of the carrier wheel and gap between the workpiece and magnet are the selected process parameters for studying the influence function. The spot (or influence function) profiles are analyzed to calculate the volume of material removal and depth of the deepest penetration (ddp) using 3D noncontact profilometer. The maximum contribution is made by wheel speed on the volume of material removal and depth of the deepest penetration. To observe the effect of selected parameter setting on the surface topography, final experimentation is performed by employing longitudinal and cross feed and it is perceived that surface generated by cross feed is more uniform.

Keywords Magnetorheological finishing · Influence function · Silicon · Material removal rate

1 Introduction

Traditional finishing processes are often unable to meet the high-quality surface specifications of the semiconductor and optical industry. Furthermore, the processes are not suitable for polishing of aspherical and freeform surfaces. It is also difficult to remove the material based on the surface error profile [1]. Single crystal silicon is used material in semiconductor industries for making IC chips and also as a substrate material for both internally and contact cooled X-ray mirrors [2, 3]. Chemo-mechanical polishing (CMP), nanogrinding [4], and single-point diamond turning (SPDT) [5] are used for finishing of silicon. However, the drawback of SPDT is the residual turning marks on finished silicon surface [3] and deterministic finishing of silicon surface is difficult to achieve by CMP, lapping, and grinding [6]. Hence, advanced polishing techniques should be adopted to overcome the disadvantages of the traditional polishing techniques. Magnetorheological finishing is an ultra-precision finishing process which is extensively used for nanofinishing of large variety of brittle materials [7].

1.1 Magnetorhelogical finishing

Magnetorheological finishing (MRF) is a computer-controlled polishing process, which is significantly used in optical lens fabrication. MRF is successfully used for figuring/final polishing of spherical/aspherical lenses and mirrors.

MRF process uses magnetorheological (MR) fluid, which consists of nonmagnetic abrasive particles, magnetic carbonyl iron particles (CIPs), carrier liquid, and some additives or stabilizers. Figure 1 shows schematic diagram of MRF process for finishing of small optics. MR fluid is deposited over the rotating carrier wheel by a nozzle and pump arrangement. When magnetic field is applied in the working gap using electromagnet or permanent magnet, MR fluid gets stiffened as its viscosity and yield stress increases and behave like a visco-plastic fluid [9]. Stiffened MR fluid ribbon proceeds towards the finishing zone by rotating carrier wheel and it abrades the workpiece. The zone of contact is restricted to a spot due to the

✉ Ajay Sidpara
ajaymsidpara@mech.iitkgp.ac.in

[1] Mechanical Engineering Department, Indian Institute of Technology Kharagpur, Kharagpur 721302, India

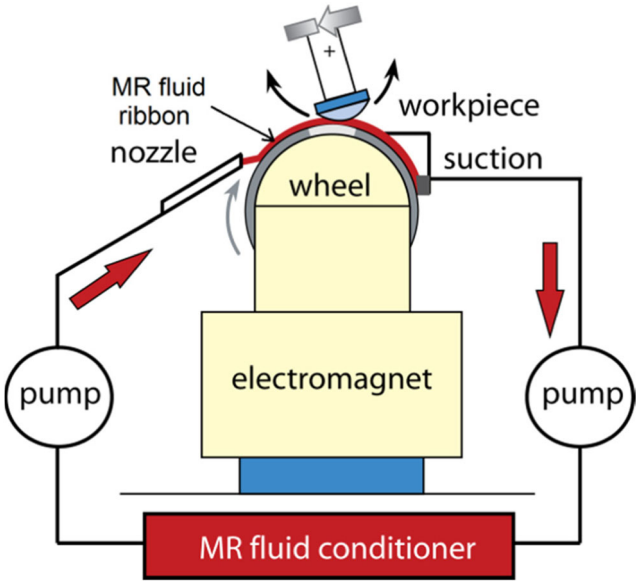

Fig. 1 Schematic diagram of magnetorheological finishing (MRF) process [8]

continuous forming of compliant sub-aperture lap. Figure 2 shows a magnified view of the finishing zone where an abrasive particle interacts with the workpiece surface [10]. When MR fluid ribbon comes in contact with the workpiece, normal force (F_n) helps the abrasive particles to penetrate in the workpiece, and tangential force (F_t) helps to shear off the peaks. Tangential force (F_t) is exerted on the workpiece surface due to rotation of the carrier wheel [11].

Normal force (F_n) mainly consists of force generated due to squeezing of MR fluid in the finishing zone and magnetic levitation force (F_m). Nonmagnetic abrasive particles move towards the workpiece surface (away from the high magnetic field) due to magnetic levitation force. The magnetic levitation force (F_m) [12] is expressed as

$$F_m = -V\mu_0 M \nabla H \tag{1}$$

where V is the volume of nonmagnetic body, M is the intensity of magnetization of magnetic fluid, μ_0 is the permeability of free space, and ∇H is the gradient of the magnetic field. Hence, abrasive particles which are trapped by CIP chain cluster interact with the workpiece surface.

1.2 Influence function

In MRF, the influence function can be described as the finishing spot which is formed during stationary finishing (without giving motion in x, y, or z direction) in a specified time as shown in Fig. 3. It contains the material removal characteristics of a finishing tool for a particular type of workpiece [14, 15]. Before final finishing experimentation, finishing procedure is assessed based on the surface error profile of workpiece and influence function of polishing tool. Figure correction capability and removal efficiency can be perceived by evaluating the finishing spot [9, 16]. It has different shapes depending on the configuration of the machine setup. Figure 3b shows a schematic diagram of general shape of influence function for the wheel type configuration of MRF setup. It is perceived that depth of deepest penetration (ddp) is situated at the minimum working gap between workpiece and carrier wheel as the MR fluid is compressed utmost here (Fig. 3c). Influence function contains the information of material removal characteristics like depth of deepest penetration, finishing area, and volume of material removed [17]. Therefore, it is utilized to remove the profile error precisely by employing x-y-z motion and rotational speed of the finishing tool [13, 18].

Higher accuracy of the influence function indicates lower residual surface profile error and better quality of the finished surface. Hence, it is conceived that the finishing quality remarkably depends on the influence function and its accurate measurement.

Influence function of wheel-based MRF configuration depends on many parameters such as magnetic field strength, MR fluid volume on the wheel, wheel speed, workpiece penetration depth in MR fluid, duration of contact, MR fluid properties (viscosity, age, constituents, etc.), and workpiece material (hardness, curvature, initial surface roughness, etc.) [13].

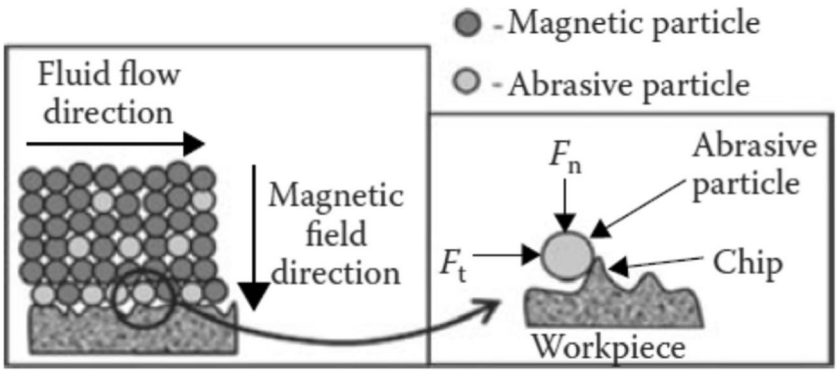

Fig. 2 Magnified view of finishing zone [10]

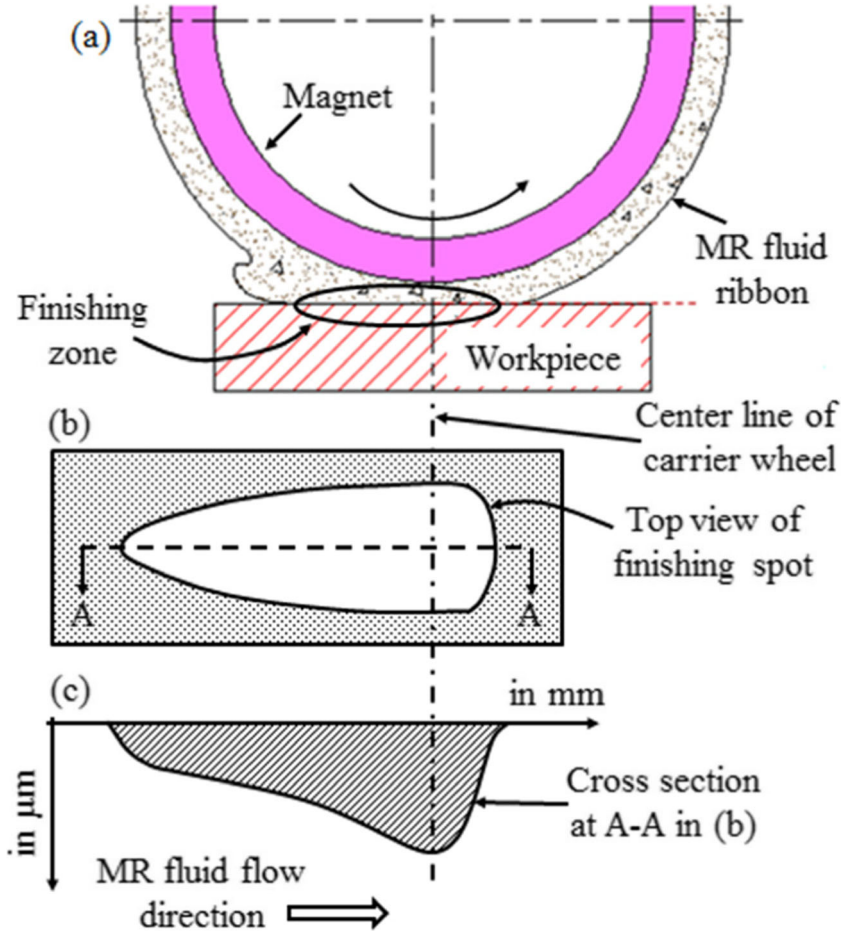

Fig. 3 **a** Schematic diagram of influence function or finishing spot. **b** Magnified top view of influence function. **c** Cross section of influence function of **b** [13]

To perceive the material removal mechanism and model the process preciously, the effect of input parameters on the responses should be studied. In this paper, central composite design of experiments and subsequent ANOVA analysis is performed to determine the effect of process parameters (wheel speed and working gap) on influence function (volume of material removed and ddp). A combination of process parameters is selected for further experimentation based on maximum material removal as well as ddp. Final experimentation is carried out by employing longitudinal and cross feed separately, and it is observed that surface produced by cross feed is more uniform.

2 Experimentation

MRF experimental setup is mounted on a four-axis CNC milling machine (PCNC 1100, Tormach, USA) as shown in Fig. 4a. The carrier wheel, which consists of a ring-shaped permanent magnet and magnet fixture, is mounted on horizontal head of the machine as shown in Fig. 4c. Sintered Nd–Fe–B permanent magnet (N42 grade, outer diameter = 100 mm, thickness = 8 mm) is used for magnetization of the MR fluid, which has maximum energy product (BH_{max}) of 40–43 MGOe. In this present study, MR fluid consists of CIPs of average particle size 1.1 μm (HQ grade from BASF, Germany), cerium oxide (CeO_2) powder as abrasive of particle size 1.1–1.8 μm (Universal Photonics Inc., USA), glycerol as a stabilizer, sodium carbonate as a buffer (Na_2CO_3), and deionized water. Concentrations of these constituents are given in Table 1. Na_2CO_3 (pH near about 11) retards the corrosion of CIPs in the alkaline environment and impedes the particles to be agglomerate because the particles become charged and mutually repulsive [19]. MR fluid is deposited on the rotating carrier wheel, and it forms a ribbon-like compliant finishing tool as shown in Fig. 3b. The width and height of the ribbon is measured, which is 8.5 and 2 mm, respectively. The MR fluid ribbon is dragged into the finishing zone by the rotating carrier wheel, and it interacts with the workpiece, which results in material removal. It is observed by the previous researchers [2] that the quality of MR fluid (in terms of yield stress and viscosity) deteriorates after each cycle. Hence, MR fluid is removed from the carrier wheel after each cycle and fresh MR fluid is loaded (approximately 35–40 g) for getting next influence function. A

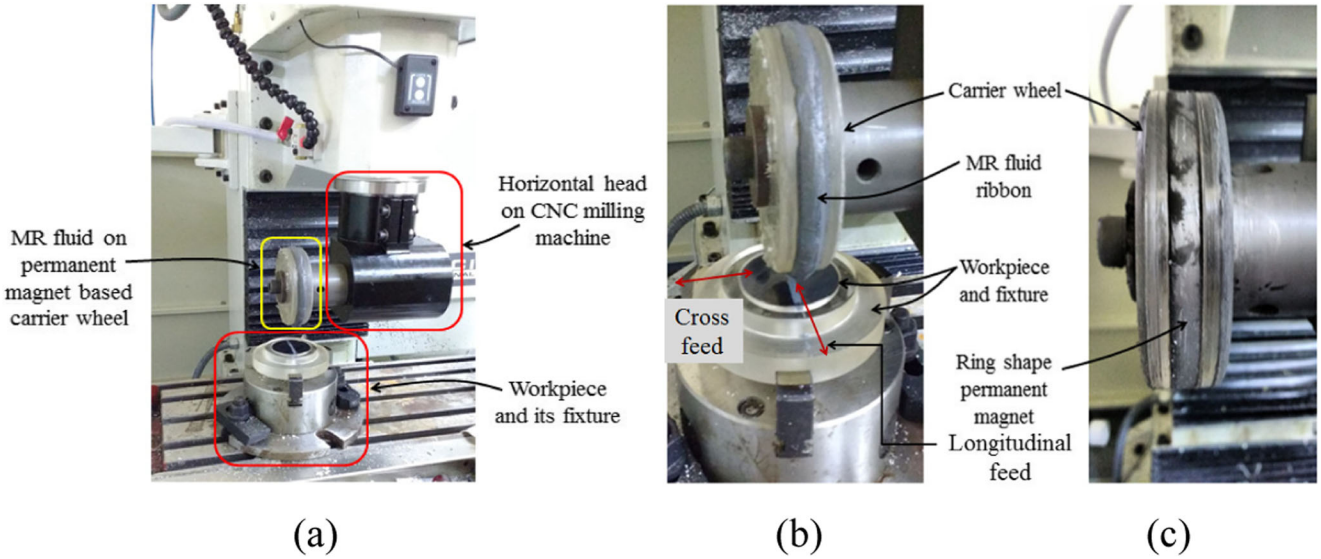

Fig. 4 **a** MRF experimental setup on four-axis CNC milling machine. **b** Carrier wheel with MR fluid. **c** Carrier wheel without MR fluid

circular blank of single crystal silicon (Crystal Techno, Russia, Ø50.8 × 6 mm) is chosen as a workpiece material. Properties of single crystal silicon are given in Table 1. No feed is given to the tool or workpiece for influence function experiments and finishing time is fixed as 10 min.

Table 1 Properties of single crystal silicon

Parameters	Value
Optical	
Transmission range	1.2 to 15 μm
Refractive index	3.4223 at 5 μm
Reflection loss	51.0% at 5 μm (two surfaces)
dn/dT	160×10^{-6}/K
dN/dμ = 0	10.4 μm
Index of absorption	1×10^{-3} cm^{-1} at 3 μm
Physical	
Density	2.33 g/cm^3
Melting point	1420 °C
Thermal conductivity	163.3 Wm^{-1} K^{-1} at 273 K
Thermal expansion	4.15×10^{-6}/°C
Hardness	Knoop 1150
Specific heat capacity	703 J/(kg K)
Dielectric constant	13 at 10 GHz
Young's modulus (*E*)	131 GPa
Shear modulus (*G*)	79.9 GPa
Bulk modulus (*K*)	102 GPa
Elastic coefficients	C_{11} = 167 MPa, C_{12} = 65 MPa, C_{44} = 80 MPa
Poisson ratio	0.266
Chemical	
Solubility	Insoluble in water
Molecular weight	28.09
Class/structure	Cubic diamond, Fd3m

Wheel speed and working gap are selected as major process parameters. Central composite design of experiment (CCD) is used to plan the experiment. The process parameters along its levels are presented in Table 2. Total of 13 experiments are carried out to gather the information about influence functions. The profiles of the influence functions are characterized using 3D noncontact profilometer (CCI MP, Taylor Hobson, UK) to calculate the volume of material removed and ddp as explained in the next section. Plan of experimentation and corresponding responses are shown in Table 3.

3 Results and discussions

Design of experiments and the responses are shown in Table 2. Regression analysis is conducted to fit the response functions with the experimental data using Design-Expert software. The adequacies of the developed quadratic models are tested using ANOVA analysis. The quadratic models for material removal rate and ddp are given in Eqs. (2) and (3), respectively.

$$\mathrm{MRR}\left(\mathrm{mm}^3/\mathrm{min}\right) = 1.06085\text{-}0.000934\,\mathrm{N}\text{–}1.0975\,\mathrm{W}\text{–}0.00018\,\mathrm{NW} + 0.00000073\,\mathrm{N}^2 + 0.5192\,\mathrm{W}^2\left(\mathrm{R}^2 = 0.94\right) \quad (2)$$

$$\mathrm{ddp}\ (\mu\mathrm{m}) = 714.95\text{-}0.68\,\mathrm{N}\text{-}728.66\mathrm{W}\text{-}0.026\mathrm{NW} + 0.00043\,\mathrm{N}^2 + 321.94\,\mathrm{W}^2\left(\mathrm{R}^2 = 0.95\right) \quad (3)$$

The ANOVA analysis table for MRR and ddp are shown in Tables 4 and 5, respectively.

Table 2 The levels of process parameters

Process parameters	Levels				
	$-\alpha$	−1	0	+1	$+\alpha$
Wheel speed (rpm)	760	800	900	1000	1040
Working gap (mm)	0.96	1	1.1	1.2	1.24
Fixed parameters					
CIP	40 (vol%)				
Abrasive particles	5 (vol%)				
Glycerol	4 (vol%)				
Na_2CO_3	0.74 (vol%)				
Deionized water	Balance				

Values of probability > F (or p value) less than 0.05 indicates that the quadratic model is statistically significant [20]. The coefficient of determination (R^2) is a measure of the degree of fit, and it is desirable that its value should approach to unity [20]. It is observed from the ANOVA table of MRR (Table 4) that the p values are less than 0.05; R^2 value is 0.9493. Similarly, it is also observed from Table 5 that the p values are less than 0.05; R^2 value is 0.9545 for ddp model. From the above observation, it is conceived that the proposed models can be successfully used to predict the responses within the selected levels of the input parameters. The contribution of each process parameter on the MRR and ddp is assessed by ANOVA analysis. It is observed that the contribution of wheel speed is more than the working gap on both MRR (Table 4) and ddp (Table 5). The effects of process parameters on the responses are represented using contour and 3D response surface plots as shown in Fig. 5a, b. The figures show that the increase of wheel speed increases both MRR and ddp. It also shows that the decrease of working gap increases both MRR and ddp. The increasing rate of MRR and ddp with the increase of wheel speed is greater than with the decrease of working gap.

3.1 Surface characterization

Surface profile of all the influence functions are analyzed for calculating the material removal rate and depth of deepest penetration using 3D noncontact profilometer. Figure 6a–c shows the sample of the 3D topography of influence functions of experiment number (9–11), respectively. The direction of MR fluid ribbon motion is indicated by the direction of arrow. To find the depth of deepest penetration for each influence function, 2D profile is extracted along the cross section A-A as shown in Fig. 6d–f. Therefore, height difference between the deepest point and the top surface is measured. To calculate the volume of material removed from each influence function, slicing technique (TalyMap7 software) is adopted as shown in Fig. 6g–i. The blue color in planar view of influence function (in Fig. 6g–i) represents the area of influence function. By applying slicing technique, volume of material removed is found in terms of μm^3 and further converted to mm^3. The effect of working gap and wheel speed on MRR and ddp has been discussed below.

3.2 Working gap

The distance between the workpiece and the carrier wheel surface is called working gap in this study. Distribution of magnetic flux density in the working gap and along the surface of the permanent magnet is measured using a Gaussmeter and which is shown in Fig. 7.

$Z = 0$ indicates the surface of the carrier wheel, and $Z = 0.5$, 1, 1.2 indicates that the magnetic flux density is measured at

Table 3 Plan of experimentation and corresponding responses

Experiment no.	Wheel speed (N) (rpm)	Working gap (W) (mm)	Volume of material removed (mm^3)	MRR (mm^3/min)	Depth of deepest penetration (ddp) (μm)
1	760	1.10	0.371	0.0370	10.262
2	800	1.20	0.413	0.0413	12.283
3	800	1.00	0.674	0.0674	21.717
4	900	1.24	0.489	0.0489	12.923
5	900	1.10	0.538	0.0538	13.576
6	900	1.10	0.559	0.0559	13.952
7	900	1.10	0.543	0.0543	14.104
8	900	0.96	0.728	0.0728	23.573
9	1000	1.20	0.712	0.0712	24.154
10	1000	1.00	1.045	0.1045	34.631
11	1040	1.10	0.929	0.0929	30.534
12	900	1.10	0.551	0.0551	13.764
13	900	1.10	0.546	0.0546	13.840

Table 4 ANOVA for MRR

Source	Sum of squares	*df*	Mean square	*F* value	*p* value probability > *F*	Percent of contribution
Model	0.004200	5	0.000850	26.19	0.0002	
N	0.002700	1	0.002700	81.94	0.0001	61.73
W	0.001100	1	0.001100	33.55	0.0007	25.27
NW	0.000013	1	0.000013	0.40	0.5475	0.31
N^2	0.000360	1	0.000360	11.13	0.0125	8.38
W^2	0.000180	1	0.000180	5.61	0.0412	4.22

0.5, 1, and 1.2 mm away from the carrier wheel surface. It is observed from Fig. 7 that the magnetic flux density is inversely proportional to working gap. It is also perceived that its value varies from the maximum at the two edges to the minimum at the center of the magnet. Hence, the workpiece will experience higher magnetic field at the lower working gap and vice versa. The intensity of magnetization (*M*) also increases at the lower working gap. The magnetic interaction force (*F*) [21] between two CIPs can be described by Eq. (4).

$$\mathrm{F} = \frac{\mu_0 \pi}{9}\left(\frac{\mathrm{r}^2 \mathrm{CM}}{\mathrm{R}'}\right)^2 \tag{4}$$

where *r* is the radius of a CIP, R' is the distance between the center of two CIPs, and *C* is the collect coefficient.

Therefore, magnetic interaction force (*F*) also increases at lower working gap due to increase in magnetization. Hence, yield stress (stiffness) of the MR fluid increases and more stiffened MR fluid ribbon interacts with the work surface and the workpiece experiences higher finishing force [22]. As a result, material removal increases at lower working gap. Furthermore, as the working gap decreases, squeezing of MR fluid increases, which further increase the hydrodynamic pressure on the work surface [11]. Thus, workpiece experiences higher force, and as a result, material removal increases.

Finite element analysis (FEA) is carried out to reveal the magnetic flux distribution over the work surface (at $Z = 1$ mm) using Maxwell v13 software as shown in Fig. 7b. The magneto-static field simulator solves for the magnetic vector potential (A) in the following field equation (Eq. (5)) based on Maxwell's equations as given by Eqs. (6) and (7).

$$\nabla \times \left(\frac{1}{\mu_r \mu_0} \nabla \times A\right) = J \tag{5}$$

where μ_0 is the permeability of free space and μ_r is the relative permeability of material.

$$\nabla \times H = J \tag{6}$$

where *H* is the magnetic field.

$$\nabla \times B = 0 \tag{7}$$

where *B* is the magnetic flux density.

J is the DC current density field flowing in the direction of transmission. Excitation (magnetic field) is provided by permanent magnet in the present case. Boundary conditions are imposed by supplying the coercive field force H_c (915 kA/m) and residual flux density B_r (1.3 T) of permanent magnet (N42 grade of Nd–Fe–B) along with the direction of magnetization to the solver. Ten numbers of passes are given to the adaptive setup with 30% refinement per pass as convergence criterion. Given the magnetic field of permanent magnet as an excitation, the magnetostatic field simulator computes the magnetic vector potential (A) at all points in space. After A is

Table 5 ANOVA for ddp

Source	Sum of squares	*df*	Mean square	*F* value	*p* value probability > *F*	Percent of contribution
Model	686.29	5	137.26	29.36	0.0001	
N	357.07	1	357.07	76.38	0.0001	50.54
W	153.06	1	153.06	32.74	0.0007	21.69
NW	0.27	1	0.27	0.059	0.8156	0.04
N^2	125.89	1	125.89	26.93	0.0013	17.82
W^2	70.05	1	70.05	14.98	0.0061	9.91

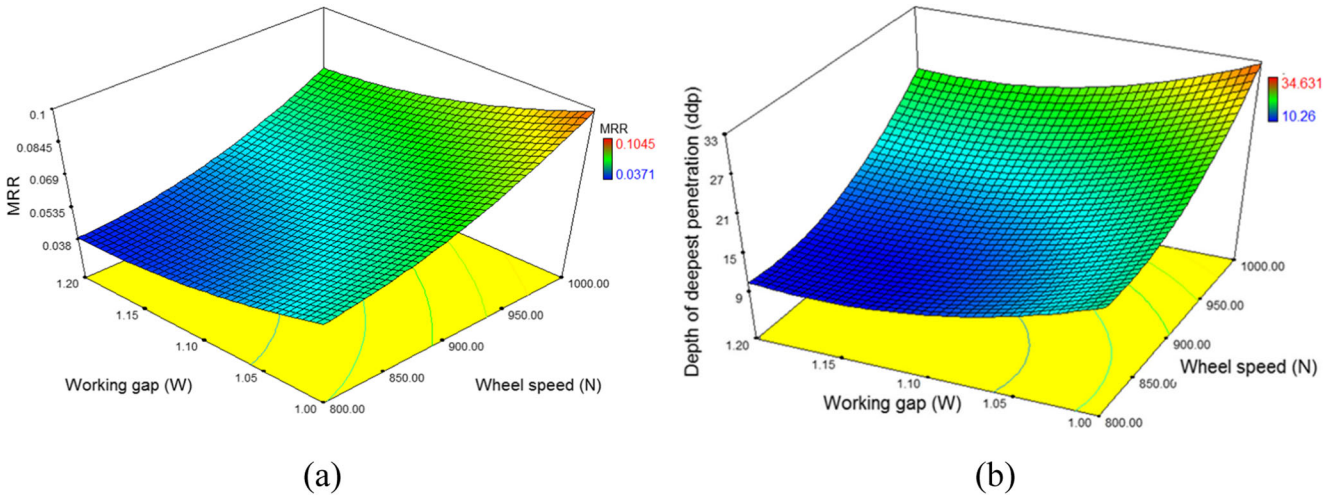

Fig. 5 3D response surfaces curves showing the interactions of process parameters with **a** MRR and **b** ddp

computed, magnetic flux density (B) and magnetic field (H) can then be calculated using the relationships of Eqs. (8) and (9), respectively.

$$B = \nabla \times A \tag{8}$$

$$B = \mu_0 H \tag{9}$$

A vibrating sample magnetometer is used to measure the magnetic properties (saturation magnetization, coercive magnetic field, residual flux density) of MR fluid. Nonlinear permeability of MR fluid is obtained from the B-H curves for the simulation. All the inputs (properties of MR fluid, workpiece, and permanent magnet) are supplied to the FEA solver and simulation is carried out.

It is observed from Fig. 7b that the magnetic flux density is maximum at the two edges of the magnet. Similar trend is also observed by measuring the actual magnetic flux density in the working gap as shown in Fig. 7a. Hence, MR fluid stiffness would be more at the two ends of the magnet compared to the middle portion of it. Hence, strong interaction between MR fluid ribbon and workpiece surface is expected below of the two ends of the permanent magnet, which results in higher material removal as shown in Fig. 6a–c. After immidiate leaving from the finishing zone, more amount of MR fluid is deposited at the two ends of the magnet. As a results, two narrow channels are formed at the trailing edge of the influence function as shown in Fig. 6a–c.

If the working gap decreases, the MR fluid is squeezed more and the ribbon gets flatted, which increases hydrodynamic pressure on the workpiece surface. As a consequence, normal force is uniformly distributed. Shape of influence function also may become uniform.

3.3 Wheel speed

MR fluid ribbon is firmly attached to the outer surface of the carrier wheel due to the high magnetic flux density. Furthermore, it is presumed that it moves with same speed as carrier wheel considering no slip between MR fluid ribbon and magnet surface. Preston's equation is the most fundamental equation to evaluate the polishing processes [23]. Kordonski et al. [24] have rewritten the Preston's equation as follows:

$$\mathrm{R} = \mathrm{kPU} = \mathrm{k}\frac{\mathrm{L}}{\mathrm{S}}\mathrm{U} = \mathrm{k}\frac{\mathrm{F}}{\mu\mathrm{S}}\mathrm{U} = \mathrm{k}\frac{\tau\mathrm{U}}{\mu} \tag{10}$$

where R is the removal rate, k is the Preston's coefficient, P is the applied pressure, U is the relative velocity, L is the normal load, S is the surface area, F is the frictional force between workpiece and the polishing tool, μ is the coefficient of friction, and τ is the shear stress.

Sidpara et al. [24] have reported that shear strain rate ($\dot{\gamma}$) of MR fluid increases with the increase of wheel speed. It is assumed that the MR fluid behave like Bingham plastic fluid under the application of magnetic field. Bingham plastic model can be describe as follows [25]:

$$\tau = \tau_y + \eta\dot{\gamma} \tag{11}$$

where τ is the shear stress, η is the viscosity, τ_y is the yield stress, and $\dot{\gamma}$ is the shear strain rate.

Therefore, if carrier wheel speed increases, shear rate increases. Shear stress increases with increase in shear rate as per Bingham plastic model (Eq. (11)). Finally, shear stress increases removal rate (R) as given by Eq. (10).

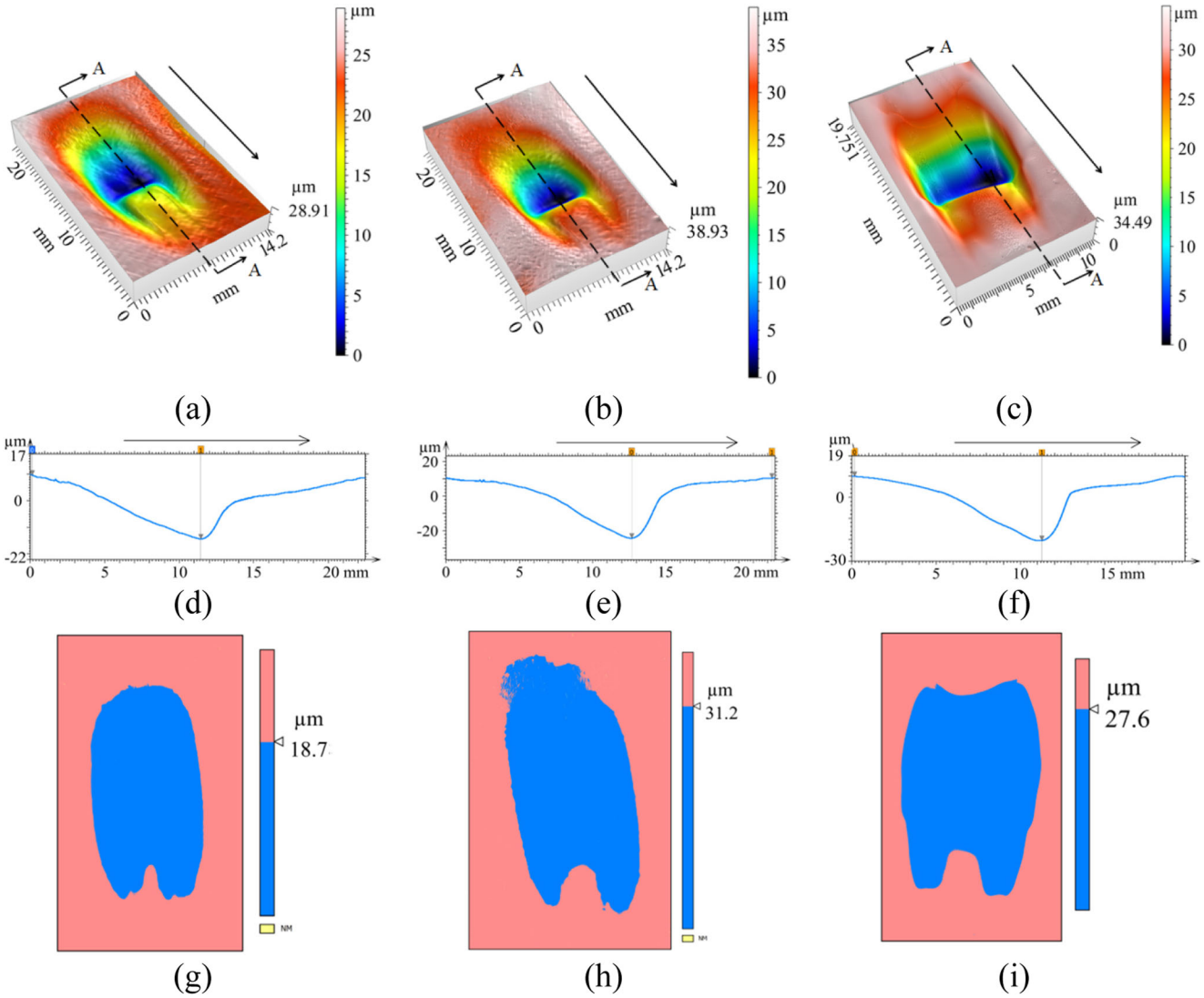

Fig. 6 **a**–**c** 3D topography of influence function of experiment number (9–11), **d**–**f** 2D surface profiles through the deepest penetration (along the cross section A-A) of **a**–**c**. **g**–**i** Planar view of influence function of **a**–**c**. Blue indicates the top view of influence function. Arrow (**a**–**f**) indicates the direction of MR fluid ribbon motion

Furthermore, when wheel speed increases, the speed of abrasive particles also increases. The tangential force (F_t) applied by the abrasive particle increases inevitably. Besides, numbers of abrasive particles coming in contact with the workpiece surface also increases in a given time (frequency of interaction increases). Thus, material removal rate increases.

Apart from that, more amount of MR fluid in a given time tries to pass through the fixed working gap that leads to more squeezing of MR fluid and normal force as well as material removal increases accordingly. But after a certain speed of the wheel, destruction of the CIP chains becomes more prominent. These separated CIPs chains are not able to exert enough force on the workpiece as compared to joined or clustered CIPs chains. As a result, forces decrease at very high rotational speed of the tool.

3.4 Final material removal region

From Table 3, it is observed that 1000-rpm wheel speed and 1-mm working gap leads to the maximum material removal rate as well as ddp. Based on the above observation, this parameter setting is selected for further experimentation. To observe the effect of selected parameter setting on the surface topography, final experimentation is performed by employing longitudinal and cross feed. The direction of longitudinal feed and cross feed is shown in the MRF experimental setup (Fig. 4b).

Feed rate 4 mm/min is used for both longitudinal and cross feed experimentations. Effect of longitudinal and cross feed on the 3D topography of the material removal region is shown in Fig. 8a, b, respectively. 2D cross-sectional profile of Fig. 8a is taken along B-B and is shown in Fig. 8c. It is observed from Fig. 8c that the profile is not uniform and material removal

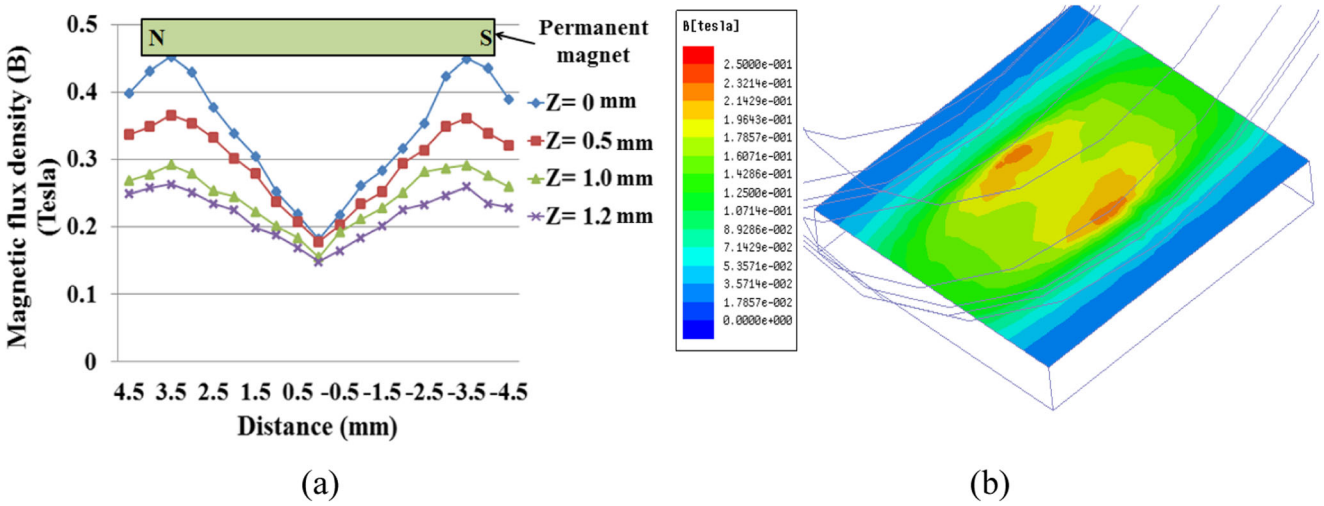

Fig. 7 **a** Distribution of magnetic flux density (B) in the working gap (Z working gap in mm). **b** Finite element analysis of magnetic field distribution on the workpiece at $Z = 1$ mm

have taken place at the two ends far more than the middle portion. This phenomenon is expected and it is due to the presence of higher magnetic flux density at the two ends of permanent magnet, which is discussed in the previous section and shown in Fig. 7a, b. Moreover, after squeezing of the MR fluid ribbon, during leaving the finishing zone, the MR fluid is attracted more towards to the ends. Reshaping of MR fluid ribbon to make uniform distribution of MR fluid over the carrier wheel is difficult to obtain. Hence, when longitudinal feed is employed, the region at below of middle portion of magnet has less stiffness. As a result, material removal decreases at the middle portion compared to the end portions.

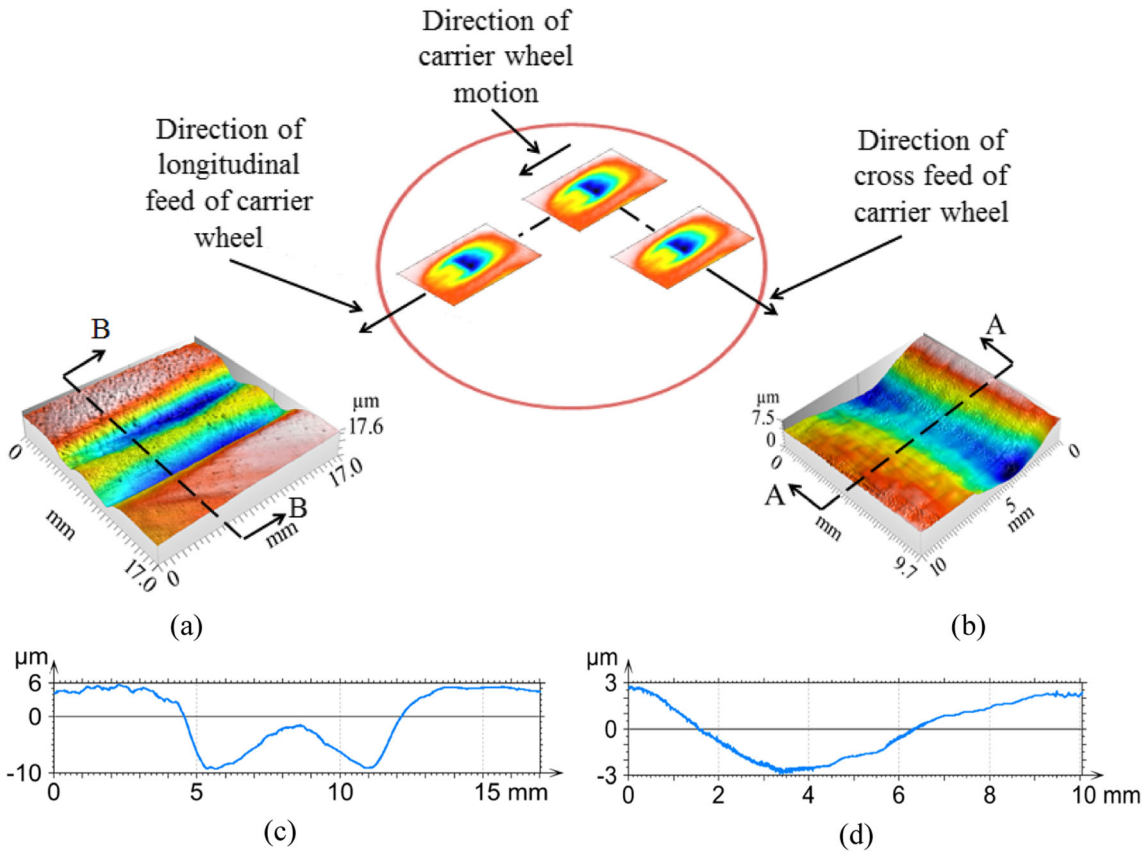

Fig. 8 Effect of feed direction on the shape of the material removal region. 3D topography of the material removal region by giving **a** longitudinal feed and **b** cross feed of the carrier wheel. 2D cross-sectional profile of **a**, **b** along **c** B–B and **d** A–A

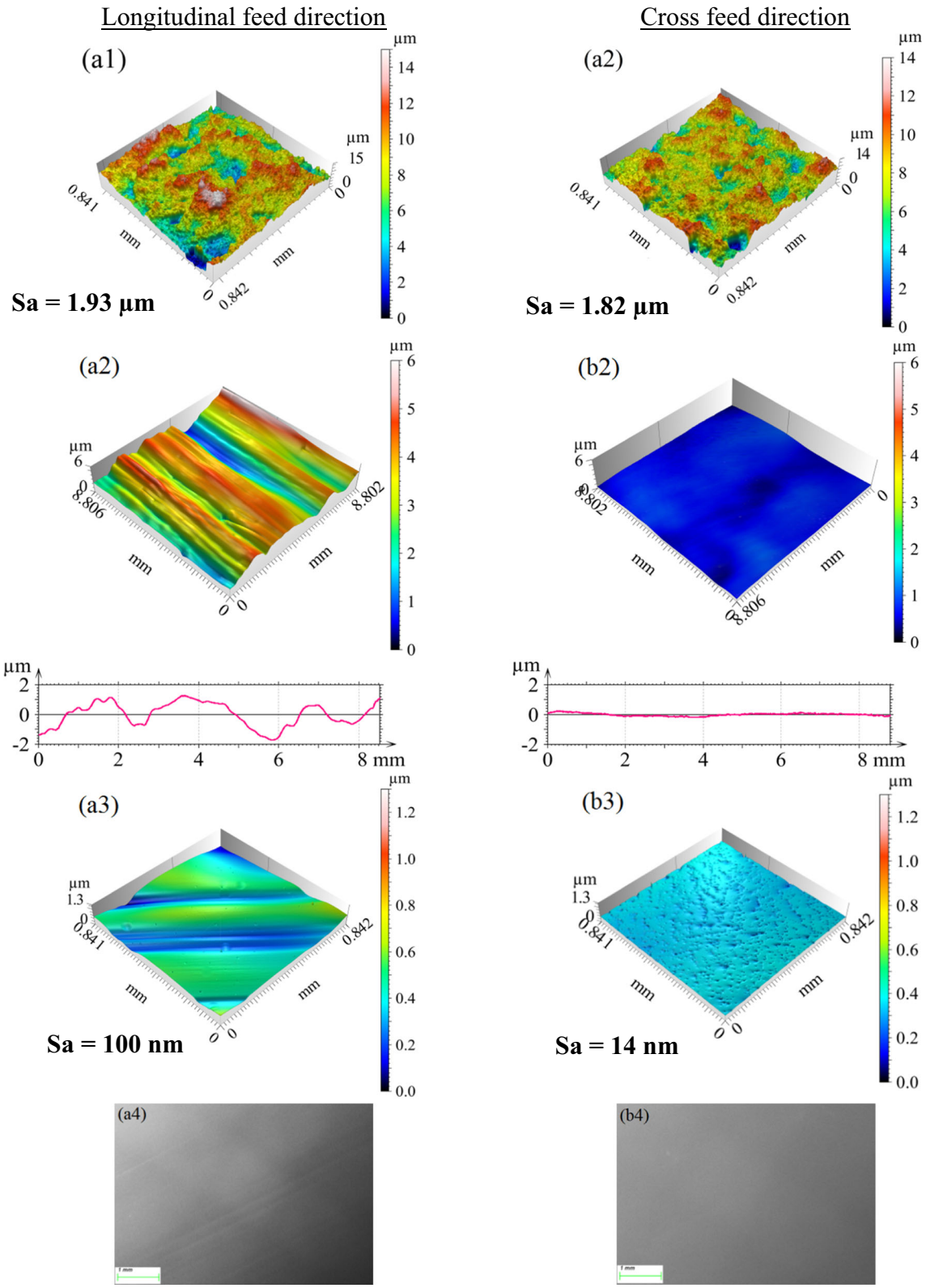

Fig. 9 **a1**, **b1** 3D topography of as-received workpiece. **a2**, **b2** 3D topography and 2D surface profile of larger finished area. **a3**, **b3** 3D topography of surface with smaller finished area. **a4**, **b4** SEM micrographs of finished surfaces. **a**, **b** stand for longitudinal feed and cross feed directions, respectively

2D cross-sectional profile of Fig. 8b is taken along A-A and is shown in Fig. 8d. It is perceived that this 2D profile is more uniform as compare to Fig. 8c. When the cross feed is employed, the direction of tangential velocity of MR fluid ribbon and the direction of tool movement are perpendicular to each other as shown in Figs. 4b and 8. Hence, irregularity produced by the middle portion of the magnet is sheared off by the more stiffened MR fluid near to the end of magnet during passing over through the irregularity. As a result, uniform profile is revealed. It is observed that the depth of the material removal region by cross feed is less than the previous one as continuous profile is generated, which may lead to the better surface finish.

From the above observation, whole surface of single crystal silicon (Ø50.8) having (111) plane is finished using the above two directions of feed rate. Overlapping step is selected as 3 mm to reduce the ripple formation and to improve the surface finish based on the profiles shown in Fig. 8c, d. Figure 9a1, a2 shows the 3D topography and areal surface roughness (S_a) of as-received samples used for the experiments with longitudinal feed and cross feed, respectively. It possesses an areal surface roughness (S_a) of 1.93 and 1.82 μm, respectively. It is observed that the surface ripples are reduced to a large extent when cross feed is given to the carrier wheel (Fig. 9b2) as compared to longitudinal feed (Fig. 9a2). As a result, S_a is reduced to 14 nm in case of cross feed (Fig. 9b3) while longitudinal feed direction gives 100 nm S_a (Fig. 9a3), which is very high in comparison. Substantial ripple formations are evident in scanning electron microscopic (SEM) images of finished surface with longitudinal feed direction (Fig. 9a4). No significant finishing marks are visible on the surface finished by employing cross feed of the carrier wheel (Fig. 9b4). Therefore, it is conceived that more uniform surface with very high surface finish can be attained by engaging cross feed of the carrier wheel.

4 Conclusions

An experimental investigation is performed to study the effect of process parameters, i.e., wheel speed and working gap on influence function during MR finishing of single crystal silicon. From the preceding results and discussion, the following conclusions are drawn:

- Working gap and wheel speed have significant effect on MRR and ddp of the influence function.
- MRR and ddp both increases with the increase of wheel speed and with decrease of working gap.
- The maximum contribution is observed by wheel speed on the MRR (70.11%) and ddp (68.36%) of influence function, while working gap has 29.49% on MRR and 31.6% on working gap.
- The 1000-rpm wheel speed and 1-mm working gap leads to the higher MRR and ddp as compared to other parameter settings.
- During final finishing experimentation, the surface profile generated employing cross feed to the tool is more uniform compared to the longitudinal feed.
- Areal surface roughness (S_a) is reduced to 14 nm in case of cross feed while longitudinal feed direction gives 100 nm S_a.
- It can be concluded that surface can be finished more uniformly by employing raster scan with cross feed to the tool.

5 Remarks

This paper is a revised and expanded version of the paper entitled "Understanding of influence function in magnetorheological fluid based finishing of single crystal silicon" presented at AIMTDR-2016 in COEP, Pune, on 16 December 2016.

Acknowledgements The authors acknowledge the funding support from the Indian Institute of Technology Kharagpur under ISIRD grant, Board of Research in Nuclear Sciences (BRNS) under young scientist research award (34/20/10/2015/BRNS).

References

1. Schinhaerl M, Smith G, Geiss A, Smith L, Rascher R, Sperber P, Pitschke E, Stamp R (2007) Calculation of MRF influence functions, Proc. SPIE 6671, Opt Manuf Test VII, 66710Y; https://doi.org/10.1117/12.730806.
2. Sidpara A, Jain VK (2012) Nano–level finishing of single crystal silicon blank using magnetorheological finishing process. Tribol Int 47:159–166
3. Tricard M, Dumas PR, Golini D (2004) New industrial applications of magnetorheological finishing (MRF). Frontiers in optics. OSA technical digest (CD), Paper OMD1. Optical Society of America; https://doi.org/10.1364/OFT.2004.OMD1.
4. Huang H, Wang BL, Wang Y, Zou J, Zhou L (2008) Characteristics of silicon substrates fabricated using nanogrinding and chemo-mechanical-grinding. Mater Sci Eng A 479:373–379
5. Shibata T, Fujii S, Makino E, Ikeda M (1996) Ductile- regime turning mechanism of single crystal silicon. Precis Eng 18(2–3): 129–137
6. Hallock B, Dumas P, Shorey A, Tricard M (2004) Recent advances in deterministic low-cost finishing of sapphire windows. Proceedings of SPIE 5786: 154–64
7. Shorey AB, Jacobs SD, Kordonski WE, Gans RF (2001) Experiments and observations regarding the mechanisms of glass removal in magnetorheological finishing. Appl Opt 40:20–33
8. Jacobs SD, Arrasmith SA, Kozhinova IA, Gregg LL, Shorey AB, Ramanofsky HJ, Golini D, Kordonski WI, Hogan S (2000) An Overview of Magnetorheological Finishing (MRF) for Precision

Optics Manufacturing (Invited Contribution). Ceram Trans 10:185–200.
9. Arrasmith SR, Kozhinova IA, Gregg LL, Shorey AB, Romanofsky HJ, Jacobs SD, Golini D, Kordonski WI, Hogan SJ, Dumas P (1999) Details of the polishing spot in magnetorheological finishing (MRF). Proc. SPIE 3782, Opt Manuf Test III, 92–100; https://doi.org/10.1117/12.369175.
10. Sidpara A, Das M, Jain VK (2009) Rheological characterization of magnetorheological finishing fluid. Mater Manuf Process 24:1467–1478
11. Sidpara A, Jain VK (2011) Experimental investigations into forces during magnetorheological fluid based finishing process. Int J Mach Tools Manuf 51:358–362
12. Rosenweig RE (1985) Ferrohydrodynamics. Dover, New York
13. Sidpara A, Jain VK (2017) Magnetorhelogical finishing. In: Jain VK (ed) Nanofinishing science and technology: Basic and Advanced finishing and polishing process. CRC Press, USA
14. Schinhaerl M, Geiss A, Rascher R, Sperber P, Stamp R, Smith L, Smith G, Pitschke E (2006) Coherences between influence function size, polishing quality, and process time in magnetorheological finishing. Proc. SPIE 6288, Current Developments in Lens Design and Optical Engineering VII, 62880Q1–9; https://doi.org/10.1117/12.678720.
15. Pitschke E, Schinhaerl M, Sperber P, Rascher R, Stamp R, Smith M, Smith L (2006) Correlation between influence-function quality and predictability of a computer-controlled polishing process. Opt Eng 45(6):063401
16. Schinhaerl M, Smith G, Stamp R, Rascher R, Smith L, Pitschke E, Sperber P, Geiss A (2008) Mathematical modelling of influence functions in computer-controlled polishing: part I. Appl Math Model 32(12):2888–2906
17. Schinhaerl M, Rascher R, Stamp R, Smith G, Smith L, Pitschke E, Sperber P (2007) Filter algorithm for influence functions in the computer controlled polishing of high-quality optical lenses. Int J Mach Tools Manuf 47(1):107–111
18. Schinhaerl M, Schneider F, Rascher R, Vogt C, Sperber P (2010) Relationship between influence function accuracy and polishing quality in magnetorheological finishing. Proc SPIE 7655, 5th International Symposium on Advanced Optical Manufacturing and Testing Technologies: Advanced Optical Manufacturing Technologies, 76550Y
19. Jacobs SD, Kordonski W, Prokhorov IV, Golini D, Gorodkin GR, Strafford DT (1998) Magnetorheological fluid composition. US Patent 5,804,095
20. Montgomery DC (2009) Design and analysis of experiments, 7th edn. John Wiley and Sons, Inc
21. Huang J, Zhang JQ, Liu JN (2005) Effect of magnetic field on properties of MR fluid. Int J Mod Phys B 19:597–601
22. Sidpara A, Jain VK (2012) Experimental investigations into surface roughness and yield stress in magnetorheological fluid based Nano-finishing process. Int J Precis Eng Manuf 13:855–860
23. Preston FW (1927) The theory and design of plate glass finishing machines. J Soc Glas Technol 11:214
24. Sidpara A, Jain VK (2014) Rheological properties and their correlation with surface finish quality in MR fluid-based finishing process. Mach Sci Technol 18:367–385
25. Sidpara A, Jain VK (2011) Effect of fluid composition on nanofinishing of single-crystal silicon by magnetic field-assisted finishing process. Int J Adv Manuf Technol 55:243–252